Full Length Article

Thermochemical splitting of CO_2 using solution combustion synthesized lanthanum–strontium–manganese perovskites

Gorakshnath Takalkar [a], Rahul R. Bhosale [a,*], Fares AlMomani [a], Suliman Rashid [a], Hazim Qiblawey [a], Mohammed Ali Saleh Saad [a], Majeda Khraisheh [a], Gopalakrishnan Kumar [b], Ram B. Gupta [c], Rajesh V. Shende [d]

[a] Department of Chemical Engineering, College of Engineering, Qatar University, P. O. Box – 2713, Doha, Qatar
[b] Institute of Chemistry, Bioscience and Environmental Engineering, Faculty of Science and Technology, University of Stavanger, Box 8600 Forus, 4036 Stavanger, Norway
[c] Department of Chemical and Life Science Engineering, Virginia Commonwealth University, Richmond, VA 23284, United States
[d] Department of Chemical and Biological Engineering, South Dakota School of Mines and Technology, Rapid City, SD 57701-3995, United States

ARTICLE INFO

ABSTRACT

Redox reactivity of $La_{(1-x)}Sr_xMnO_3$ (LSM) perovskites towards a solar thermochemical CO_2 splitting (CS) cycle is investigated. The LSM perovskites are synthesized via a solution combustion synthesis (SCS) method using glycine as the reducing agent. Multiple analytical techniques are used for the structural characterization of the LSM perovskites. Thermogravimetric thermal reduction (TR) and CS cycles (in three sets: one, three and ten cycles) are conducted to estimate the amounts of O_2 released (n_{O_2}) and CO produced (n_{CO}) by each LSM perovskite. Higher n_{O_2} by each LSM perovskite, as compared to the n_{CO} during the first cycle. The n_{O_2} is decreased, and the re-oxidation capacity of each LSM perovskite is improved from cycle one to three. In terms of the average n_{O_2} and n_{CO} from cycle 2 to cycle 10, the $La_{0.60}Sr_{0.41}Mn_{0.99}O_{2.993}$ (214.8 μmol of O_2/g·cycle) and $La_{0.30}Sr_{0.70}Mn_{0.99}O_{2.982}$ perovskites (342.1 μmol of CO/g·cycle) are observed to have the uppermost redox reactivity. The redox reactivity of all the LSM perovskites (except for $La_{0.88}Sr_{0.11}Mn_{1.00}O_{2.980}$) is recorded to be higher than that of the widely studied CeO_2 material.

1. Introduction

Meeting the ever-increasing worldwide demand for energy by using solar fuels produced via H_2O (WS)/CO_2 splitting (CS) reactions is one of the feasible approaches for harnessing the renewable and profusely available solar energy [1,2]. This process exploits the concentrated solar power to drive the high-temperature thermal reduction (TR) of metal oxides (MOs) [3]. Effectively, by applying this technology, the storage of solar energy in the form of chemical energy is possible [4,5]. This stored chemical energy is preferred as it can be transported and stockpiled for a long time without any degradation. Recently, Marxer et al. [6] developed a first of its kind pilot-scale set up for the production of 700 L of solar syngas via 291 stable redox cycles.

According to the studies so far, the process efficiency of the thermochemical WS/CS process heavily depends on the redox properties of the MOs [7]. The desirable characteristics of a good MO include high

H_2/CO yield, faster TR and re-oxidation (RO) kinetics, lower cycle time, higher thermal stability over multiple cycles, elevated O_2 diffusion rates from the surface to the bulk of the MO, and a smaller temperature difference between the TR and RO steps. The redox materials investigated for both WS and CS reactions include volatile MOs such as zinc oxide [8–10] and tin oxide [11,12], and non-volatile MOs for instance, iron oxide [13–15], ferrites [16–19], doped ceria [20–23], and hercynite [24,25]. Among these, ceria and doped ceria appears to be a beneficial choice, as these oxides possess the anticipated material properties.

In recent years, perovskite-based oxides [26–28] were investigated for thermochemical WS/CS reactions with an assumption that they will outperform ceria. Among these perovskites, the La-Sr-Mn-based (LSM) perovskites were inspected for the production of both H_2 and CO via WS and CS cycles. For the TR temperature range of 1523 to 1923 K, the $La_{0.7}Sr_{0.3}MnO_3$ (LSM30) and $La_{0.6}Sr_{0.4}MnO_3$ (LSM40) perovskites showed higher TR yield as compared to ceria [29]. According to Yang

et al. [30], the La$_{1-x}$Sr$_x$MnO$_3$ materials (x = 0 to 0.5) represented a higher TR yield as a function of an increase in the atomic concentration of Sr. Demont and Abanades [31] synthesized and tested the La$_{0.35}$Sr$_{0.65}$MnO$_{3-\delta}$, La$_{0.5}$Sr$_{0.5}$MnO$_{3-\delta}$, La$_{0.65}$Sr$_{0.35}$MnO$_{3-\delta}$, and La$_{0.8}$Sr$_{0.2}$MnO$_{3-\delta}$ towards the CS reactions (in one cycle) and reported La$_{0.5}$Sr$_{0.5}$MnO$_{3-\delta}$ as the best choice for producing a maximum amount of O$_2$ (n_{O_2} = 195 µmol/g·cycle) and CO (n_{CO} = 242 µmol/g·cycle). Dey and Rao [32] studied the La$_{1-x}$Sr$_x$MnO$_3$ (x = 0.3, 0.4, and 0.5) towards splitting of CO$_2$ at isothermal operating conditions and observed high CO production (n_{CO} = 134 µmol/g·cycle) by La$_{0.5}$Sr$_{0.5}$MnO$_3$ at 1400 °C (partial pressure of O$_2$ = 10^{-5} atm and partial pressure of CO$_2$ = 1 atm). Dey and Rao [32] further reported that the La$_{0.5}$Sr$_{0.5}$MnO$_3$ was capable of producing ~three times higher CO than the CeO$_2$ at 1500 °C. As per the several studies, the rise in the Sr content was responsible for an increase in the reduction extent and decreased in the re-oxidation yield [29,31,33–38].

As per the literature review, selected LSM compositions were investigated for solar thermochemical fuel production. It is essential to find the finest combination of LSM perovskite, which is capable of producing the maximum amount of solar fuel in multiple thermochemical cycles. In this regard, this work concentrates on the exploration of the TR and RO behavior of the LSM perovskites, i.e., La$_{(1-x)}$Sr$_x$MnO$_3$ (where x = 0.1 to 0.9) in multiple CS cycles (Fig. 1). This study will assist in improving the understanding and rational design for the application of LSM perovskites for WS/CS reactions and in comparing them with the CeO$_2$.

2. Experimental sections

2.1. Chemicals

La(NO$_3$)$_3$·6H$_2$O (99.99% trace metal basis), Mn(NO$_3$)$_2$·4H$_2$O (purum p.a., ≥97.0%), and Sr(NO$_3$)$_2$ (ACS reagent, ≥99.0%) were obtained from Sigma Aldrich, USA, and used as received. De-ionized water (ultrapure Type 1 from Direct-Q system, Millipore, France) was consumed for the preparation of the solution containing metal precursors and glycine. Ultra-high pure Ar and CO$_2$-Ar (50:50) were obtained from Buzwair Gases, Qatar.

2.2. Synthesis of LSM perovskites

Synthesis of the LSM perovskites was carried out via a glycine based solution combustion synthesis (SCS) method. In a typical recipe,

calculated amounts of precursors (to prepare 1 g of the LSM perovskites) [39] were dissolved in 50 ml of deionized water along with the glycine (fuel to precursor ratio = 1). As-prepared solution was then pre-heated up to 300 °C (exposed to air) by using a temperature-controlled hot plate. A viscous gel comprised of the precursors and glycine was obtained after complete evaporation of the water. The combustion reaction was propagated as the temperature of the gel was increased up to the auto-ignition temperature. As-synthesized powder of the LSM perovskites was crushed using pestle and mortar and further calcined up to 1000 °C in the air for 4 h using a muffle furnace. Table 1 reports the abbreviations assigned to each LSM perovskite derived via the SCS method. By using the powder X-ray diffractometer (PXRD, PANalytical XPert MPD/DY636), the phase composition of the LSM perovskites was determined. The scanning electron microscope (SEM, Nova Nano 450, FEI, 200kx) equipped with the energy-dispersive X-ray spectroscopy (EDS) was utilized to identify the elemental composition and material morphology.

2.3. CO$_2$ splitting experiments

Multiple thermochemical experiments were conducted by using a high-temperature SETSYS Evolution TGA (Setaram Instruments, France) (Fig. 2). Details allied with the TGA set-up were already reported elsewhere [40]. A platinum pan was placed inside the furnace (surrounded by an alumina tube) to support the reference and the sample alumina (100 µl) crucibles. The flowrates of the gases were monitored and controlled by using mass flow controllers, and the temperature was regulated by using a Pt–Rh type-B thermocouple. Thermogravimetric CS experiments were carried out by using approximately 50 mg of the LSM perovskite powder. The drift in the mass of the LSM perovskite during the TR (at 1400 °C for 60 min, 100 ml/min Ar), and CS (1000 °C for 30 min, 100 ml/min of 50% CO$_2$/Ar mixture) steps were recorded by using the Calisto software. Based on the variation in the mass during both steps and following equations, the amounts O$_2$ released (n_{O_2}) and CO produced (n_{O_2}) by each LSM perovskite were estimated.

$$n_{O_2} = \frac{\Delta m_{loss}}{(M_{O_2} \times m_{LSM})} \tag{1}$$

$$n_{CO} = \frac{\Delta m_{gain}}{(M_O \times m_{LSM})} \tag{2}$$

In the above equations, the Δm_{loss} and Δm_{gain} represents the loss and gain in the mass of the LSM perovskites during the TR and CS steps. The molecular weights of the O and O$_2$ are represented as M_O and M_{O2}. Likewise, the amount of LSM perovskite used during the TGA experiments is presented as M_{LSM}. TGA blank runs (performed by using empty crucible) were subtracted from the TGA actual experiments (conducted by using the LSM perovskites) to avoid the effect of the thermal buoyancy.

Fig. 1. Schematic of LSM based solar thermochemical fuel production process.

Table 1
Abbreviations assigned and the chemical composition of the LSM perovskites (prepared via SCS and calcined at 1000 °C in the air for 4 h).

Abbreviation	La/Sr/Mn (as-prepared)	La/Sr/Mn (from EDS)	Composition
LSM10	0.90/0.10/1.00	0.88/0.11/1.00	La$_{0.88}$Sr$_{0.11}$Mn$_{1.00}$O$_{2.98}$
LSM20	0.80/0.20/1.00	0.81/0.21/1.01	La$_{0.81}$Sr$_{0.21}$Mn$_{1.01}$O$_{3.04}$
LSM30	0.70/0.30/1.00	0.68/0.30/1.01	La$_{0.68}$Sr$_{0.30}$Mn$_{1.01}$O$_{2.98}$
LSM40	0.60/0.40/1.00	0.60/0.41/0.99	La$_{0.60}$Sr$_{0.41}$Mn$_{0.99}$O$_{2.99}$
LSM50	0.50/0.50/1.00	0.52/0.49/1.00	La$_{0.52}$Sr$_{0.49}$Mn$_{1.00}$O$_{3.02}$
LSM60	0.40/0.60/1.00	0.41/0.59/0.98	La$_{0.41}$Sr$_{0.59}$Mn$_{0.98}$O$_{2.97}$
LSM70	0.30/0.70/1.00	0.30/0.70/0.99	La$_{0.30}$Sr$_{0.70}$Mn$_{0.99}$O$_{2.98}$
LSM80	0.20/0.80/1.00	0.21/0.78/1.01	La$_{0.21}$Sr$_{0.78}$Mn$_{1.01}$O$_{3.01}$
LSM90	0.10/0.90/1.00	0.09/0.91/1.00	La$_{0.09}$Sr$_{0.91}$Mn$_{1.00}$O$_{2.99}$

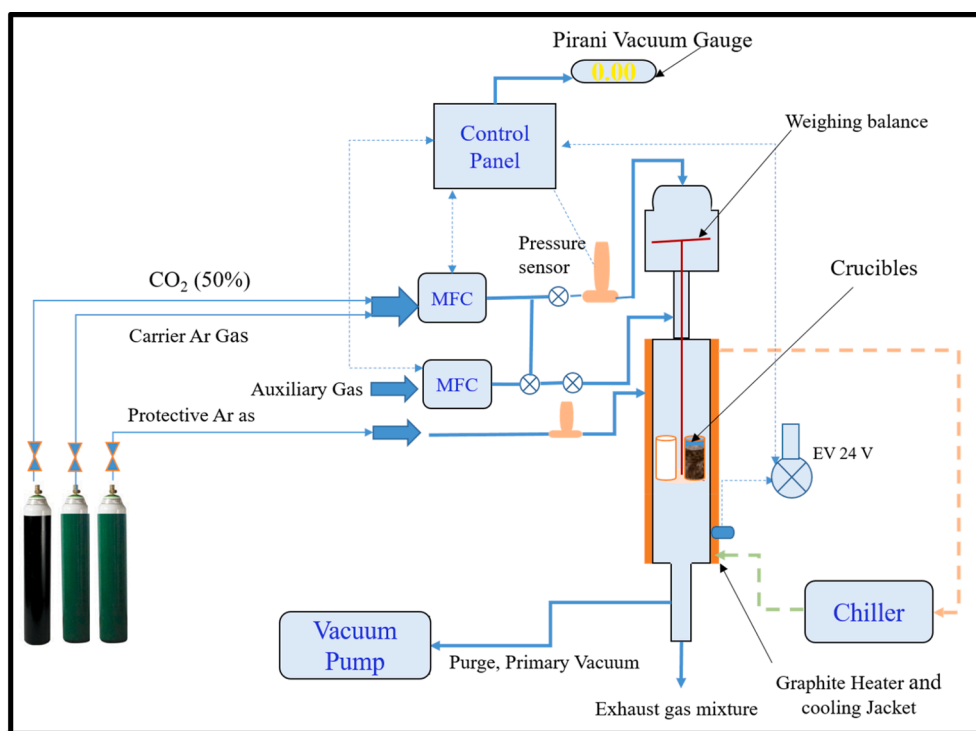**Fig. 2.** Experimental set-up used for the evaluation of the LSM perovskites.

3. Results and discussion

The phase composition of the SCS synthesized LSM perovskites were identified by performing the PXRD analysis. The PXRD peaks, presented in Fig. 3, shows nominally phase pure LSM perovskites with no evidence of any impurities such as La-, Mn-, Sr-based individual oxides, or La, Sr, Mn metals. As the crystal ionic radii of Sr (132 pm) is higher than that of La (117.2 pm), the increase in the atomic concentration of the Sr resulted in a shift in the PXRD peaks towards higher 2θ angle. This observation provided further confirmation of the successful synthesis of LSM perovskites via the SCS method. The PXRD peaks reported in Fig. 3 matched very well with the PXRD findings reported in previous studies [41]. By employing the Scherrer formula, the average crystallite size of all LSM perovskites was estimated to be in the range of 50 to 70 nm.

In addition to the PXRD, by using the SEM/EDS instrument, the elemental composition of each LSM perovskite was verified. The EDS results were observed to be consistent with the findings reported by the PXRD analysis. The EDS patterns associated with the LSM20, LSM40, LSM60, and LSM80 perovskites (exemplified) are presented in Fig. 4. Besides, the atomic concentrations of La, Sr, and Mn, and the chemical composition of each LSM perovskite identified by using the EDS patterns are reported in Table 1.

In order to examine the microstructural morphology of the LSM perovskites, SEM analysis was conducted. The representative images obtained for LSM20, LSM40, LSM60, and LSM80 perovskites are shown in Fig. 5. The drift in the La and Sr atomic concentrations had an insignificant effect on the LSM morphology. However, as the images were taken at different locations (for each LSM), we cannot wholly neglect the chances of having dissimilar/disordered images. The SEM analysis showed that all the LSM perovskites possess a porous
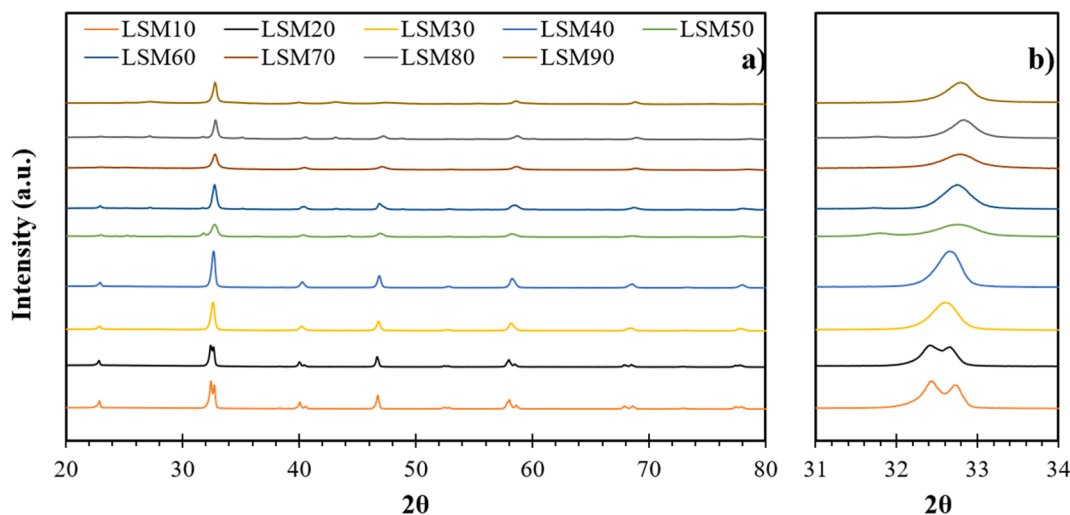

Fig. 3. PXRD patterns of LSM perovskites, a) 2θ = 20° to 80° and b) 2θ = 31° to 34° (prepared via SCS and calcined at 1000 °C in the air for 4 h).
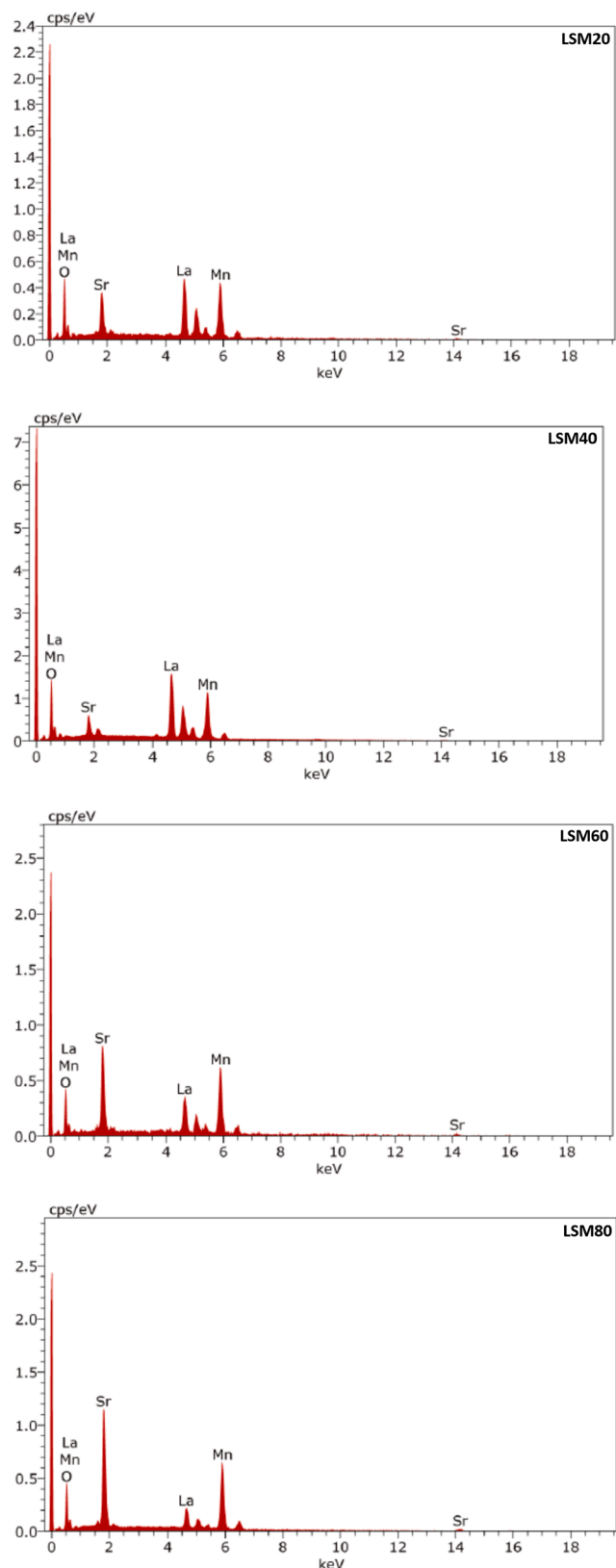
Fig. 4. EDS patterns of LSM20, LSM40, LSM60, and LSM80 (prepared via SCS and calcined at 1000 °C in the air for 4 h).

morphology.

We have first tested the redox performance of the SCS synthesized LSM perovskites in one thermochemical CS cycle. In thermochemical cycles, the mass of a MO decreases during the TR step due to the release of lattice O_2. In contrast, due to the gain of O_2, the mass of the MO increases during the re-oxidation step. The mass of each LSM perovskite was decreased as a function of the increase in the TR temperature (T_H) and the reaction time during the TR step (Fig. 6). In terms of the mass loss, the LSM50 perovskite reached its plateau after attaining the TR temperature of 1400 °C. In contrast, the remaining LSM perovskites continued to lose weight throughout the entire TR step. By considering that the TR starts at 800 °C, the kinetics was quickest for LSM90 and the slowest for the LSM10 perovskite. Furthermore, from 800 °C to 1400 °C (dwell time equal to 60 min), the %Δm_{loss} was highest for LSM90 perovskite (~6.8%) and lowest in the case of the LSM10 perovskite (~0.65%).

The TGA profiles obtained in case of each LSM perovskite (during the TR step) were translated into the n_{O_2} by using Eq. (1). The numbers reported in Fig. 7 indicate that the n_{O_2} by the LSM90 perovskite was the greatest as compared to other LSM perovskites. For instance, the n_{O_2} by LSM90 perovskite (1476.6 μmol/g) was higher by 1298.7, 1243.5, 1003.5, 932.0, 885.9, 866.7, 828.3, and 675.0 μmol/g when compared to the LSM10, LSM20, LSM30, LSM40, LSM50, LSM60, LSM70, and LSM80 perovskites, respectively. The inclusion of Sr^{+2} as a partial substitute for La^{+3} on A-site (from x = 0.1 to 0.9) results into a deviation in the oxidation state of Mn from +3 to +4. Because of this drift, the LSM perovskites (with higher Sr content) seems to be favorable towards TR reaction as compared to the LSM perovskites with the lower Sr content.

The thermally decomposed LSM perovskites were further examined towards CS step at 1000 °C for 30 min. Fig. 8 represents the TGA profiles associated with the first CS step. As mentioned earlier, it was expected that the mass of the MO would rise due to the re-oxidation. As per the expectation, as shown in Fig. 8, the mass of each LSM perovskite was increased during the CS step. Close inspection of these TGA profiles indicates that the LSM70 and LSM50 perovskites exhibited the quickest RO rates. At the same time, the LSM90 perovskite showed the slowest RO kinetics. Obtained results further show that the LSM70 perovskite attained the maximum mass gain, and the LSM90 perovskite indicated the lowest increase in the mass during the first CS step. With the help of the obtained TGA profiles and Eq. (2), the calculated n_{CO} by each LSM perovskite is presented in Fig. 9. The LSM70 perovskite displayed the highest CO production (424.0 μmol/g), and the LSM90 displayed the lowest n_{CO} (64.7 μmol/g) in cycle 1. The LSM40, LSM60, and LSM80 perovskites indicated approximately identical n_{CO} in the range of 285.7 to 309.5 μmol/g. Likewise, the LSM20 and LSM30 perovskites produced ~162.0 μmol of CO/g in cycle 1. The authors would like to admit that it is difficult to know the exact reason for such results as the TGA set-up only provides the information related to the mass variations.

The overall analysis of the 1st thermochemical cycle indicate that the n_{CO} produced by the LSM perovskites were lower than the n_{O_2}. The probable reasons for such trends are a) all the LSM perovskites were freshly prepared and never underwent any thermal cycling before performing the first TR step, and b) all the LSM perovskites have not reached their thermal stability during cycle 1. It was highly essential to know if the LSM perovskites show a similar trend in additional cycles. Hence, these redox materials were further scrutinized by performing three consecutive cycles (Fig. 10).

Table 2 report the calculated n_{O_2} and n_{CO} by each LSM perovskite during three cycles. The numbers listed shows that the n_{O_2} by all LSM perovskites decreased considerably in cycle 2. For example, the n_{O_2} by LSM10, LSM30, LSM50, LSM70, and LSM90 was reduced by 117.6, 292.1, 465.4, 402.5, and 1133.4 μmol/g in cycle 2 as compared to cycle 1. The results reported in Table 2 further shows that, except for LSM30, LSM80, and LSM90 perovskites, most of the LSM perovskites underwent a drop in the CO production capacity in cycle 2. The n_{CO} by LSM10, LSM20, LSM40, LSM50, LSM60, and LSM80 diminished by 19.1, 34.9,
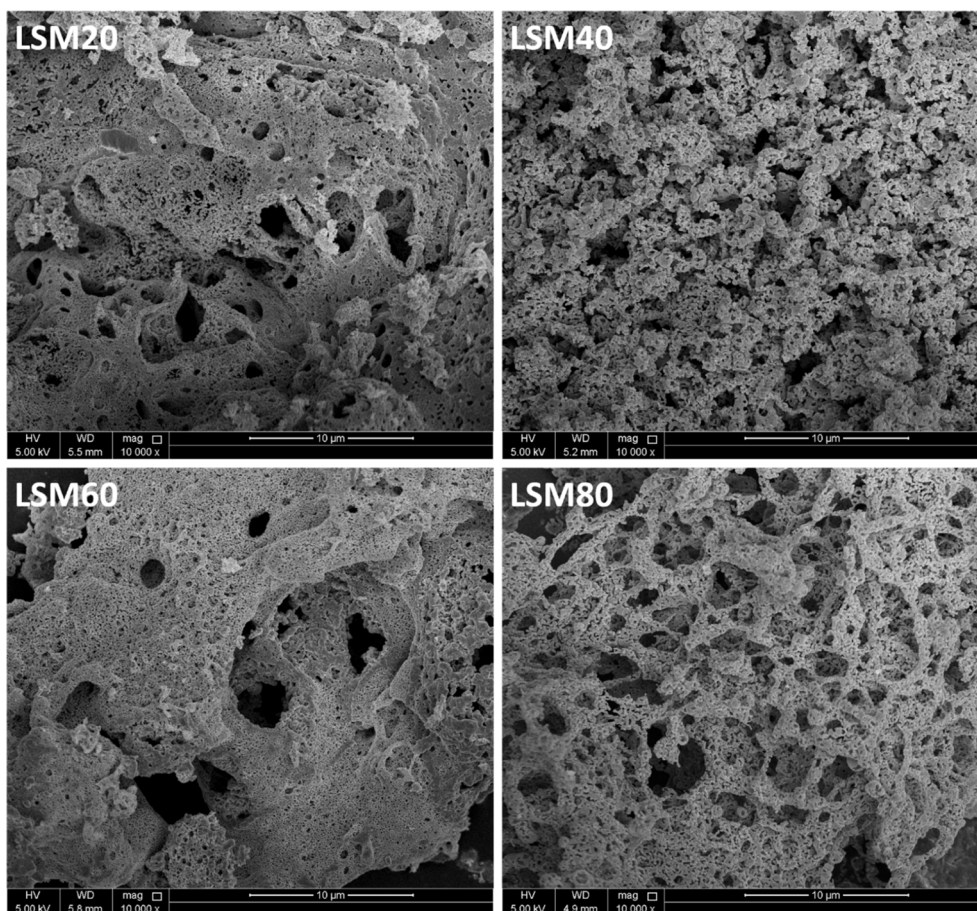
Fig. 5. SEM images of LSM20, LSM40, LSM60, and LSM80 (prepared via SCS and calcined at 1000 °C in the air for 4 h).
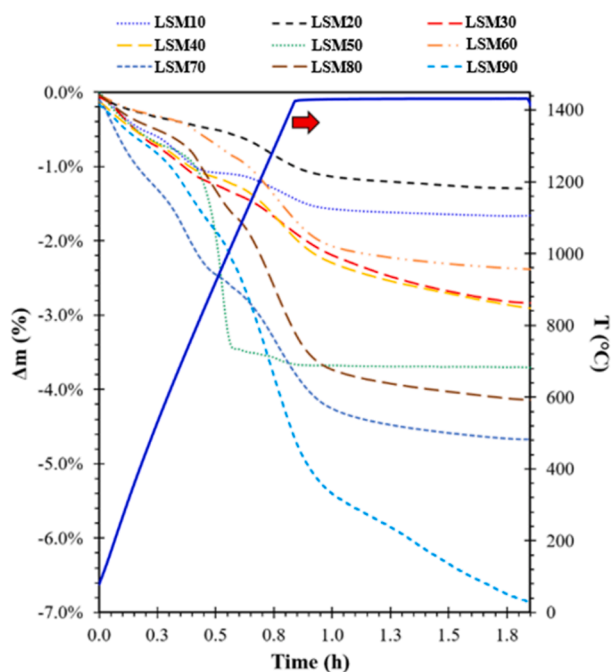

Fig. 6. LSM perovskites: TGA profiles of the first TR step (1400 °C for 60 min, heating/cooling rate = 25 °C/min).
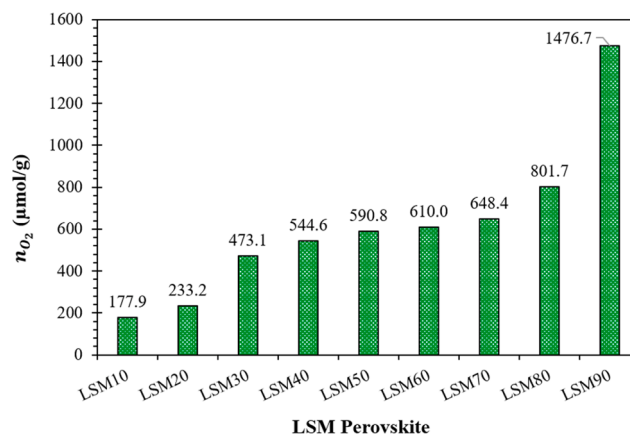

Fig. 7. n_{O_2} by LSM perovskites during 1st TR step (1400 °C for 60 min, heating/cooling rate = 25 °C/min).

17.9, 100.7, 17.9, and 61.5 µmol/g, individually in cycle 2 as compared to the first cycle. In case of the LSM60 and LSM80 perovskites, the n_{CO} during cycle 2 enhanced by 40.9 and 19.2 µmol/g (as compared to cycle 1), whereas in the case of LSM50 perovskite, n_{CO} remained steady during both cycles. A higher n_{CO}/n_{O_2} ratio accomplished by all the LSM perovskites during cycle 2. For instance, the n_{CO}/n_{O_2} ratio for LSM10, LSM20, LSM30, LSM40, LSM50, LSM60, LSM70, LSM80, and LSM90 upsurged by 0.936, 0.569, 0.783, 0.371, 1.324, 1.433, 0.821, 1.198, and 0.201 in cycle 2 when compared with the n_{CO}/n_{O_2} attained in cycle 1.

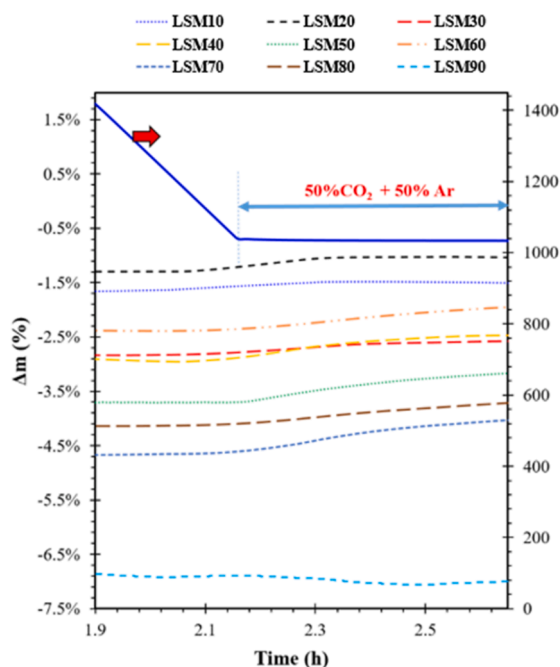Cycle 3 marked a further reduction in the TR capacity of all the LSM

Fig. 8. LSM perovskites: TGA profiles obtained during the first CS step (1000 °C for 30 min, heating/cooling rate = 25 °C/min).
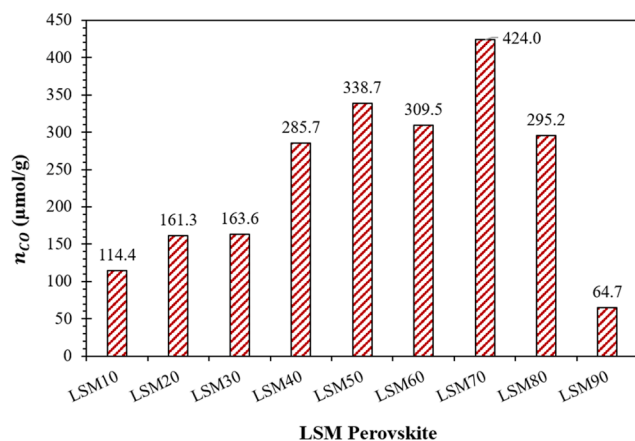
Fig. 9. n_{CO} by LSM perovskites during the 1st CS step (1000 °C for 30 min, heating/cooling rate = 25 °C/min).

perovskites (except for LSM50). The n_{O_2} decreased by 26.3%, 37.0%, 17.7%, 25.4%, 8.9%, 25.9%, 22.9%, and 42.5% in cycle 3 for LSM10, LSM20, LSM30, LSM40, LSM60, LSM70, LSM80, and LSM90, individually in comparison to the n_{O_2} in cycle 2. Likewise, the CS ability of LSM10, LSM20, and LSM60 perovskites reduced by 13.3%, 6.9%, and 7.1% in cycle 3 as compared to cycle 2. In contrast, the n_{CO} by LSM50, LSM70, and LSM80 perovskites remained stable and the n_{CO} by LSM30, LSM40, and LSM90 perovskites increased by 17.1%, 5.0%, and 79.4%, respectively, in cycle 3, when paralleled with cycle 2. Overall, the n_{CO}/n_{O_2} ratio for LSM10, LSM20, LSM30, LSM40, LSM50, LSM60, LSM70, LSM80, and LSM90 upsurged by 0.28, 0.60, 0.48, 0.36, 0.01, 0.04, 0.48, 0.43, and 0.52, respectively in 3rd cycle when matched to the n_{CO}/n_{O_2} ratios reported for the 2nd cycle.

The results obtained during three consecutive cycles indicate a reduction in the n_{O_2} by all the LSM perovskites. In contrast, an upsurge in the n_{CO}/n_{O_2} ratio was noticed for all the LSM perovskites from cycle 1 to cycle 3. The probable reason for these results is the transformation of the redox reactivity of the selected LSM perovskites from an unstable zone
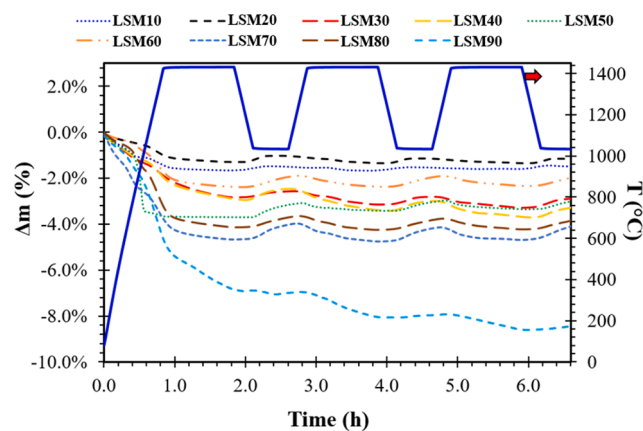

Fig. 10. LSM perovskites: TGA profiles obtained during three cycles (TR at 1400 °C for 60 min, CS at 1000 °C for 30 min, and heating/cooling rate = 25 °C/min).

(cycle 1) to a more stable zone (cycle 3). This probably happened as the LSM perovskites underwent three thermal cyclings. After the 3rd cycle, it is believed that some of the LSM perovskites have improved their thermal stability and redox reactivity towards the TR and CS reactions.

To determine the worthiest combination of the LSM perovskite, which can attain a stable production of CO for a longer duration, this study was further extended towards performing ten successive thermochemical cycles. Fig. 11 presents the TGA profiles obtained (experimental time ~22 h) during ten thermochemical CS cycles. As each LSM perovskite has behaved differently towards the multiple TR and CS steps, the TGA profiles reported for all LSM perovskites (Fig. 11) look different than each other. To avoid the misrepresentation of the data, the average n_{O_2}, n_{CO}, and n_{CO}/n_{O_2} ratio was hereafter calculated by excluding the first cycle (which is deemed as the most unstable zone). Similar to the previous sections, the TR (Fig. 12) and CS (Fig. 13) capacity of all the LSM perovskites, from cycle 2 to cycle 10, estimated by using Eqs. (1) and (2).
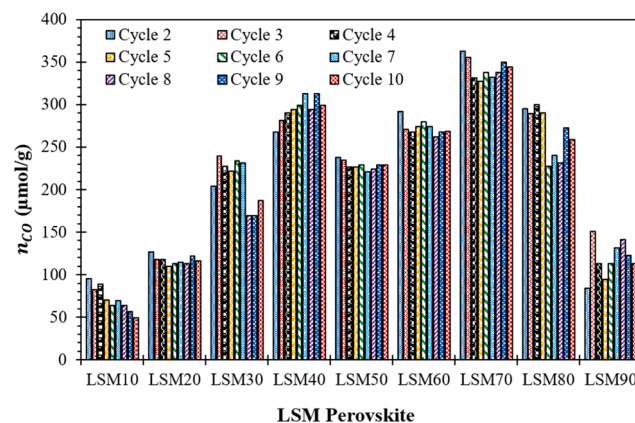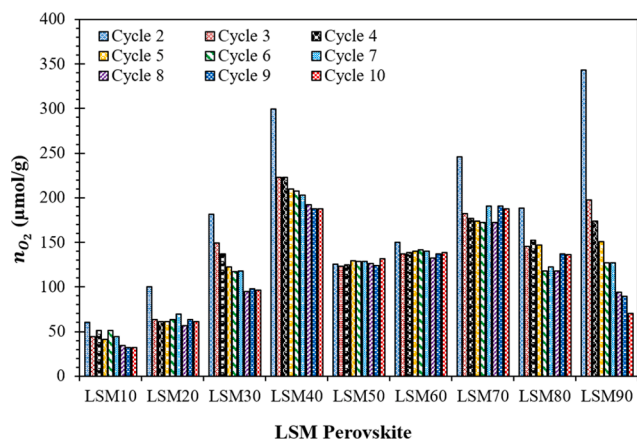
According to Fig. 12, the n_{O_2} by LSM10, LSM30, LSM40, and LSM90 perovskites reduced from cycle 2 to cycle 9, whereas the TR capacity of the LSM80 perovskite was inconsistent. In contrast, a stable n_{O_2} by LSM20, LSM50, LSM60, and LSM70 perovskites from cycle 2 to cycle 10. In terms of numbers, the average n_{O_2} by each LSM perovskite can be arranged as: LSM40 (214.8 μmol/g·cycle) > LSM70 (187.9 μmol/g·cycle) > LSM90 (152.6 μmol/g·cycle) > LSM80 (140.5 μmol/g·cycle) > LSM60 (139.4 μmol/g·cycle) > LSM50 (126.9 μmol/g·cycle) > LSM30 (123.7 μmol/g·cycle) > LSM20 (66.6 μmol/g·cycle) > LSM10 (43.4 μmol/g·cycle). These results confirmed that the redox reactivity of the LSM20, LSM50, LSM60, and LSM70 was much better towards the TR step as compared to the remaining LSM perovskites.

According to the data reported in Fig. 13, the LSM20, LSM50, LSM60, and LSM70 perovskites exhibited stable production of CO from cycle 2 to cycle 10. Remaining perovskites showed varying amounts of CO production and especially in case of the LSM10 the n_{CO} decreased with an increase in the number of cycles. LSM perovskites can be organized, based on the average n_{CO} from cycle 2 to cycle 10, as: LSM70 (342.1 μmol/g·cycle) > LSM40 (294.6 μmol/g·cycle) > LSM60 (272.9 μmol/g·cycle) > LSM80 (267.4 μmol/g·cycle) > LSM50 (228.7 μmol/g·cycle) > LSM30 (209.4 μmol/g·cycle) > LSM90 (118.0 μmol/g·cycle) > LSM20 (116.7 μmol/g·cycle) > LSM10 (71.0 μmol/g·cycle). The listed numbers indicate that the CS ability of the LSM perovskites does not follow any specific trend. Interestingly, LSM40 perovskite again showed a higher redox potential towards producing 294.6 μmol of CO/g·cycle (the second-highest among all the LSM perovskites investigated).

The LSM perovskites were further compared with each other based on their average n_{CO}/n_{O_2} ratio from cycle 2 to cycle 10. As per the obtained data, the average n_{CO}/n_{O_2} ratio in the case of LSM60 and LSM80

Table 2

LSM perovskites: n_{O_2}, n_{CO}, and n_{CO}/n_{O_2} ratio in three cycles (TR at 1400 °C for 60 min, CS at 1000 °C for 30 min, and heating/cooling rate = 25 °C/min).

LSM	Cycle 1			Cycle 2			Cycle 3		
	n_{O_2}(μmol/g)	n_{CO}(μmol/g)	$\frac{n_{CO}}{n_{O_2}}$	n_{O_2}(μmol/g)	n_{CO}(μmol/g)	$\frac{n_{CO}}{n_{O_2}}$	n_{O_2}(μmol/g)	n_{CO}(μmol/g)	$\frac{n_{CO}}{n_{O_2}}$
LSM10	177.9	114.4	0.63	60.4	95.3	1.58	44.5	82.6	1.85
LSM20	233.2	161.3	0.69	100.2	126.4	1.26	63.2	117.7	1.86
LSM30	473.1	163.6	0.35	181.1	204.4	1.13	148.9	239.5	1.61
LSM40	544.6	285.7	0.53	299.1	267.9	0.90	223.2	281.3	1.26
LSM50	590.8	338.7	0.57	125.4	238.0	1.90	123.3	226.1	1.83
LSM60	610.0	309.5	0.51	150.3	291.7	1.94	136.9	270.8	1.98
LSM70	648.4	424.0	0.65	245.8	362.6	1.48	182.1	355.6	1.95
LSM80	801.7	295.2	0.37	188.5	295.2	1.57	145.3	289.8	1.99
LSM90	1476.7	64.7	0.05	343.3	83.9	0.25	197.5	150.5	0.76
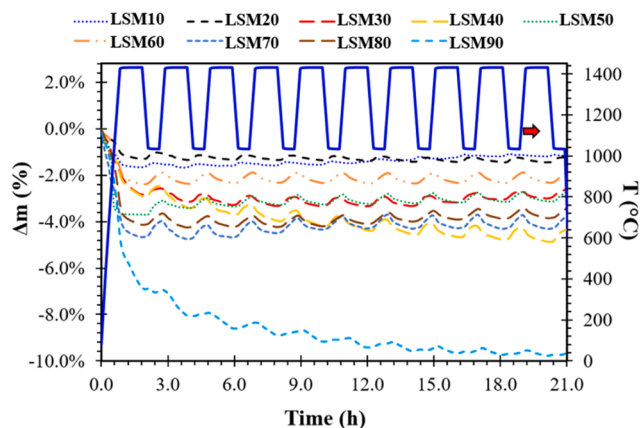
Fig. 11. LSM perovskites: TGA profiles obtained during ten cycles (TR at 1400 °C for 60 min, CS at 1000 °C for 30 min, and heating/cooling rate = 25 °C/min).

Fig. 12. n_{O_2} by LSM perovskites from cycle 2 to cycle 10 (TR at 1400 °C for 60 min, CS at 1000 °C for 30 min, and heating/cooling rate = 25 °C/min).

Fig. 13. n_{CO} by LSM perovskites from cycle 2 to cycle 10 (TR at 1400 °C for 60 min, CS at 1000 °C for 30 min, and heating/cooling rate = 25 °C/min).

Table 3

Comparison between the results recorded in this study and the findings reported by Bhosale and Takalkar [40], Dey and Rao [32] and Yang et al. [30].

Materials	TR Temp (°C)	CS Temp (°C)	n_{O_2}(μmol/g·cycle)	n_{CO}(μmol/g·cycle)
CeO$_2$ [40]	1400	1000	47.6	95.6
LSM10	1400	1000	43.4	71.0
LSM20	1400	1000	66.6	116.7
LSM30	1400	1000	123.7	209.4
LSM40	1400	1000	214.8	294.6
LSM50	1400	1000	126.9	228.7
LSM60	1400	1000	139.4	272.9
LSM70	1400	1000	187.9	342.1
LSM80	1400	1000	140.5	267.4
LSM90	1400	1000	152.6	118.0
LSM30 [32]	1400	1400	37.9	75.9
LSM40 [32]	1400	1400	48.9	98.2
LSM50 [32]	1400	1400	69.5	134.8
LSM10 [30]	1400	–	24.5	–
LSM20 [30]	1400	–	61.6	–
LSM30 [30]	1400	–	145.6	–
LSM40 [30]	1400	–	203.8	–

perovskites was the highest as compared to the other LSM perovskites. For most of the LSM perovskites (except for LSM40 and LSM90) the average n_{CO}/n_{O_2} ratio was higher than 1.6. The average n_{CO}/n_{O_2} ratio > 1.6 indicates that the re-oxidation capacity of the LSM perovskites is reduced, and further work needs to be done for its improvement. A possible option is to improve the ion mobility of the LSM perovskites via the inclusion of one or more suitable dopants in the crystal structure. Overall, the LSM perovskites, based on their average n_{CO}/n_{O_2} ratio, can be organized as: LSM60 > LSM80 > LSM70 > LSM50 > LSM20 > LSM30 > LSM10 > LSM40 > LSM90.

Table 3 reports the comparison between the LSM perovskites and

CeO$_2$ (experiments conducted at identical operating conditions). The data listed indicate that, except for LSM10 perovskite, all the LSM perovskites produced higher n_{O_2} and n_{CO} than CeO$_2$. In contrast, CeO$_2$ exhibited higher average n_{CO}/n_{O_2} ratio than most of the LSM perovskites. The elevated average n_{CO}/n_{O_2} ratio indicates that the RO

potential of CeO_2 is superior to the LSM perovskites. We believe that the CS temperature (1000 °C) and re-oxidation time (30 min) used were appropriate for the CeO_2 material to re-oxidized completely. However, the experimental conditions employed were insufficient for the LSM perovskites to regain their oxidized state.

In addition to CeO_2, the LSM perovskites investigated in this study were also compared with LSM perovskites studied by Dey and Rao [32] and Yang et al. [30]. Dey and Rao [32] tested LSM30, LSM40, and LSM50 perovskites for the thermochemical splitting of CO_2 at isothermal experimental conditions (1673 K). The amounts of O_2 released and CO produced by the LSM30, LSM40, and LSM50 perovskites investigated by us were considerably higher than the similar perovskites examined by Dey and Rao [32]. The probable reason for this lower amount of fuel production reported by Dey and Rao [32] is the lesser time (15 min) permitted for the TR step.

Yang et al. [30] examined LSM10, LSM20, LSM30, and LSM40 perovskites for the thermochemical splitting of H_2O (TR at 1400 °C and re-oxidation at 800 °C). As the aim of the presented investigation was to split the CO_2, only the results associated with the TR step (O_2 release) were compared. As the time allowed for the TR step by us and by Yang et al. [30] were comparable (especially for LSM30 and LSM40), the amount of O_2 released by LSM10, LSM20, LSM30, and LSM40 in this study was approximately identical to the TR ability of the similar perovskites reported by Yang et al. [30]. Based on the comparison with published literature, presently, we are investigating the effect of temperature and dwell time allied with both TR and CS steps to understand the long-term redox reactivity of the LSM perovskites.

4. Summary and conclusions

In this investigation, $La_{(1-x)}Sr_xMnO_3$ (where x = 0.1 to 0.9) i.e., LSM perovskites were examined towards thermochemical CS cycles. A solution combustion synthesis approach was utilized for the synthesis of LSM perovskites. Derived LSM perovskites were further characterized using PXRD, EDS, and SEM techniques. Formation of nominally phase pure LSM perovskites with no evidence of any impurities such as La-, Mn-, Sr-based individual oxides or La, Sr, Mn metals was confirmed from the PXRD and EDS analysis. The average crystallite size of all LSM perovskites was estimated to be in the range of 50 to 70 nm. The SEM analysis verified the insignificant effect of the variation in the La and Sr atomic concentrations on the porous morphology of the LSM perovskites. The CS ability of each LSM perovskite was examined by performing one, three, and ten thermochemical cycles (at a fixed $T_H = 1400$ °C and $T_L = 1000$ °C). Obtained results indicate that the rise in the Sr molar concentration is favorable to improve the TR yield of the LSM perovskites. As the number of cycles increased from two to ten, most of the LSM perovskites reached their thermal stability and produced roughly stable amounts of O_2 and CO. The long term thermal cycling (from cycle 2 to cycle 10) shows that the LSM40 perovskite was the best choice in terms of $n_{O_2} = 214.8$ μmol/g·cycle, whereas LSM70 showed the highest activity towards CS reaction ($n_{CO} = 342.1$ μmol/g·cycle). In terms of the re-oxidation ability (n_{CO}/n_{O_2} ratio), the LSM60 was observed to be the most promising choice as it is capable of attaining the highest n_{CO}/n_{O_2} ratio = 1.96. All the LSM perovskites (except LSM10) exhibited higher amount of O_2 release and CO production when compared with the ceria material. The improved fuel production capacity of the LSM perovskite will result into a higher solar-to-fuel-energy conversion efficiency.

CRediT authorship contribution statement

Gorakshnath Takalkar: Methodology, Investigation, Data curation, Writing - original draft. **Rahul R. Bhosale:** Conceptualization, Validation, Data curation, Writing - original draft, Writing - review & editing, Project administration, Funding acquisition. **Fares AlMomani:** Validation, Data curation, Writing - original draft, Writing - review & editing. **Suliman Rashid:** Methodology, Investigation. **Hazim Qiblawey:** Data curation, Writing - review & editing. **Mohammed Ali Saleh Saad:** Writing - review & editing. **Majeda Khraisheh:** Writing - review & editing. **Gopalakrishnan Kumar:** Writing - original draft. **Ram B. Gupta:** Writing - original draft. **Rajesh V. Shende:** Writing - original draft.

Declaration of Competing Interest

The authors declare that they have no known competing financial interests or personal relationships that could have appeared to influence the work reported in this paper.

Acknowledgments

References

[1] Carrillo RJ, Scheffe JR. Advances and trends in redox materials for solar thermochemical fuel production. Sol Energy 2017;156:3–20. https://doi.org/10.1016/j.solener.2017.05.032.

[2] Bhosale RR, Takalkar G, Sutar P, Kumar A, AlMomani F, Khraisheh M. A decade of ceria based solar thermochemical H2O/CO2 splitting cycle. Int J Hydrogen Energy 2019;34–60. https://doi.org/10.1016/j.ijhydene.2018.04.080.

[3] Dry ME. The Fischer-Tropsch process: 1950–2000. Catal. Today 2002;71:227–41. https://doi.org/10.1016/S0920-5861(01)00453-9.

[4] Bhosale R, Kumar A, Almomani F. Solar thermochemical hydrogen production via terbium oxide based redox reactions. Int J Photoenergy 2016. https://doi.org/10.1155/2016/9727895.

[5] Agrafiotis C, Roeb M, Sattler C. A review on solar thermal syngas production via redox pair-based water/carbon dioxide splitting thermochemical cycles. Renew Sustain Energy Rev 2015;42:254–85. https://doi.org/10.1016/j.rser.2014.09.039.

[6] Marxer D, Furler P, Scheffe J, Geerlings H, Falter C, Batteiger V, et al. Demonstration of the entire production chain to renewable kerosene via solar thermochemical splitting of H2O and CO2. Energy Fuels 2015;29:3241–50. https://doi.org/10.1021/acs.energyfuels.5b00351.

[7] Koepf E, Alxneit I, Wieckert C, Meier A. A review of high temperature solar driven reactor technology: 25 years of experience in research and development at the Paul Scherrer Institute. Appl Energy 2017. https://doi.org/10.1016/j.apenergy.2016.11.088.

[8] Steinfeld A. Solar hydrogen production via a two-step water-splitting thermochemical cycle based on Zn/ZnO redox reactions. Int J Hydrogen Energy 2002;27:611–9. https://doi.org/10.1016/S0360-3199(01)00177-X.

[9] Bhosale RR. Thermodynamic efficiency analysis of zinc oxide based solar driven thermochemical H2O splitting cycle: Effect of partial pressure of O2, thermal reduction and H2O splitting temperatures. Int J Hydrogen Energy 2018;43: 14915–24. https://doi.org/10.1016/j.ijhydene.2018.06.074.

[10] Bhosale R, Kumar A, AlMomani F, Gupta RB. Solar thermochemical ZnO/ZnSO4 water splitting cycle for hydrogen production. Int J Hydrogen Energy 2017;42: 23474–83. https://doi.org/10.1016/j.ijhydene.2017.02.190.

[11] Abanades S, Villafan-Vidales HI. CO2 and H2O conversion to solar fuels via two-step solar thermochemical looping using iron oxide redox pair. Chem Eng J 2011; 175:368–75. https://doi.org/10.1016/j.cej.2011.09.124.

[12] Bhosale RR, Kumar A, Sutar P. Thermodynamic analysis of solar driven SnO2/SnO based thermochemical water splitting cycle. Energy Convers Manag 2017;135: 226–35. https://doi.org/10.1016/j.enconman.2016.12.067.

[13] Charvin P, Abanades S, Flamant G, Lemort F. Two-step water splitting thermochemical cycle based on iron oxide redox pair for solar hydrogen production. Energy 2007;32:1124–33. https://doi.org/10.1016/j.energy.2006.07.023.

[14] Bhosale RR, Kumar A, Van Den Broeke LJP, Gharbia S, Dardor D, Jilani M, et al. Solar hydrogen production via thermochemical iron oxide-iron sulfate water splitting cycle. Int J Hydrogen Energy 2015;40:1639–50. https://doi.org/10.1016/j.ijhydene.2014.11.118.

[15] Gálvez ME, Loutzenhiser PG, Hischier I, Steinfeld A. CO2 splitting via two-step solar thermochemical cycles with Zn/ZnO and FeO/Fe3O4 redox reactions: thermodynamic analysis. Energy Fuels 2008;22:3544–50. https://doi.org/10.1021/ef800230b.

[16] Amar VS, Puszynski JA, Shende RV. H2 generation from thermochemical water-splitting using yttria stabilized NiFe2O4 core-shell nanoparticles. J Renew Sustain Energy 2015;7. https://doi.org/10.1063/1.4915312.

[17] Bhosale RR, Alxneit I, Van Den Broeke LLP, Kumar A, Jilani M, Gharbia SS, et al. Sol-gel synthesis of nanocrystalline Ni-ferrite and Co-ferrite redox materials for thermochemical production of solar fuels. Mater. Res. Soc. Symp. Proc. 2014;1675: 203–8. https://doi.org/10.1557/opl.2014.866.

[18] Scheffe JR, Li J, Weimer AW. A spinel ferrite/hercynite water-splitting redox cycle. Int J Hydrogen Energy 2010;35:3333–40. https://doi.org/10.1016/j.ijhydene.2010.01.140.

[19] Bhosale RR. Thermodynamic analysis of Ni-ferrite based solar thermochemical H 2 O splitting cycle for H 2 production. Int J Hydrogen Energy 2019:61–71. https://doi.org/10.1016/j.ijhydene.2018.03.145.

[20] Scheffe JR, Jacot R, Patzke GR, Steinfeld A. Synthesis, characterization, and thermochemical redox performance of Hf4+, Zr4+, and Sc3+ doped ceria for splitting CO2. J Phys Chem C 2013;117:24104–10. https://doi.org/10.1021/jp4050572.

[21] Takalkar GDD, Bhosale RRR, Kumar A, AlMomani F, Khraisheh M, Shakoor RAA, et al. Transition metal doped ceria for solar thermochemical fuel production. Sol Energy 2018. https://doi.org/10.1016/j.solener.2018.03.022.

[22] Le Gal A, Abanades S. Catalytic investigation of ceria-zirconia solid solutions for solar hydrogen production. Int J Hydrogen Energy 2011;36:4739–48. https://doi.org/10.1016/j.ijhydene.2011.01.078.

[23] Ehrhart BD, Muhich CL, Al-Shankiti I, Weimer AW. System efficiency for two-step metal oxide solar thermochemical hydrogen production – Part 1: Thermodynamic model and impact of oxidation kinetics. Int J Hydrogen Energy 2016;41:19881–93. https://doi.org/10.1016/j.ijhydene.2016.07.109.

[24] Muhich CL, Evanko BW, Weston KC, Lichty P, Liang X, Martinek J, et al. Efficient generation of H2 by splitting water with an isothermal redox cycle. Science (80-) 2013;341:540–2. doi: 10.1126/science.1239454.

[25] Muhich CL, Ehrhart BD, Witte VA, Miller SL, Coker EN, Musgrave CB, et al. Predicting the solar thermochemical water splitting ability and reaction mechanism of metal oxides: A case study of the hercynite family of water splitting cycles. Energy Environ Sci 2015;8:3687–99. https://doi.org/10.1039/c5ee01979f.

[26] Dey S, Naidu BS, Rao CNR. Beneficial effects of substituting trivalent ions in the B-site of La0.5Sr0.5Mn1-xAxO3 (A = Al, Ga, Sc) on the thermochemical generation of CO and H2 from CO2 and H2O. Dalt Trans 2016;45:2430–5. https://doi.org/10.1039/c5dt04822b.

[27] Nair MM, Abanades S. Experimental screening of perovskite oxides as efficient redox materials for solar thermochemical CO 2 conversion. Sustain Energy Fuels 2018;2:843–54. https://doi.org/10.1039/c7se00516d.

[28] Cooper T, Scheffe JR, Galvez ME, Jacot R, Patzke G, Steinfeld A. Lanthanum Manganite Perovskites with Ca/Sr A-site and Al B-site Doping as Effective Oxygen Exchange Materials for Solar Thermochemical Fuel Production. Energy Technol 2015;3:1130–42. https://doi.org/10.1002/ente.201500226.

[29] Scheffe JR, Weibel D, Steinfeld A. Lanthanum-strontium-manganese perovskites as redox materials for solar thermochemical splitting of H2O and CO2. Energy Fuels 2013;27:4250–7. https://doi.org/10.1021/ef301923h.

[30] Yang CK, Yamazaki Y, Aydin A, Haile SM. Thermodynamic and kinetic assessments of strontium-doped lanthanum manganite perovskites for two-step thermochemical water splitting. J Mater Chem A 2014;2:13612–23. https://doi.org/10.1039/c4ta02694b.

[31] Demont A, Abanades S. High redox activity of Sr-substituted lanthanum manganite perovskites for two-step thermochemical dissociation of CO2. RSC Adv 2014;4: 54885–91. https://doi.org/10.1039/c4ra10578h.

[32] Dey S, Rao CNR. Splitting of CO2 by Manganite Perovskites to Generate CO by Solar Isothermal Redox Cycling. ACS Energy Lett 2016;1:237–43. https://doi.org/10.1021/acsenergylett.6b00122.

[33] Dey S, Naidu BS, Rao CNR. Ln0.5A0.5MnO3 (Ln=Lanthanide, A= Ca, Sr) perovskites exhibiting remarkable performance in the thermochemical generation of CO and H2 from CO2 and H2O. Chem - A Eur J 2015;21:7077–81. doi: 10.1002/chem.201500442.

[34] Demont A, Abanades S, Beche E. Investigation of perovskite structures as oxygen-exchange redox materials for hydrogen production from thermochemical two-step water-splitting cycles. J Phys Chem C 2014;118:12682–92. https://doi.org/10.1021/jp5034849.

[35] Bork AH, Povoden-Karadeniz E, Rupp JLM. Modeling Thermochemical Solar-to-Fuel Conversion: CALPHAD for Thermodynamic Assessment Studies of Perovskites, Exemplified for (La, Sr)MnO3. Adv Energy Mater 2017;7. https://doi.org/10.1002/aenm.201601086.

[36] Kuo JH, Anderson HU, Sparlin DM. Oxidation-reduction behavior of undoped and Sr-doped LaMnO3 nonstoichiometry and defect structure. J Solid State Chem 1989; 83:52–60. https://doi.org/10.1016/0022-4596(89)90053-4.

[37] Mizusaki J, Mori N, Takai H, Yonemura Y, Minamiue H, Tagawa H, et al. Oxygen nonstoichiometry and defect equilibrium in the perovskite-type oxides La1-xSrxMnO3+d. Solid State Ionics 2000;129:163–77. https://doi.org/10.1016/S0167-2738(99)00323-9.

[38] Takalkar G, Bhosale R, AlMomani F. Combustion synthesized A0.5Sr0.5MnO3-δ perovskites (where, A = La, Nd, Sm, Gd, Tb, Pr, Dy, and Y) as redox materials for thermochemical splitting of CO2. Appl Surf Sci 2019;489:80–91. doi: 10.1016/j.apsusc.2019.05.284.

[39] Ashok A, Kumar A, Bhosale RR, Almomani F, Saleh Saad MAH, Suslov S, et al. Influence of fuel ratio on the performance of combustion synthesized bifunctional cobalt oxide catalysts for fuel cell application. Int J Hydrogen Energy 2019. https://doi.org/10.1016/j.ijhydene.2018.02.111.

[40] Bhosale RR, Takalkar GD. Nanostructured co-precipitated Ce0.9Ln0.1O2 (Ln = La, Pr, Sm, Nd, Gd, Tb, Dy, or Er) for thermochemical conversion of CO2. Ceram Int 2018;44:16688–97. doi: 10.1016/j.ceramint.2018.06.096.

[41] Gálvez ME, Jacot R, Scheffe J, Cooper T, Patzke G, Steinfeld A. Physico-chemical changes in Ca, Sr and Al-doped La-Mn-O perovskites upon thermochemical splitting of CO2 via redox cycling. Phys Chem Chem Phys 2015;17:6629–34. https://doi.org/10.1039/c4cp05898d.